DNA Gold Nanoparticle Motors Demonstrate Processive Motion with Bursts of Speed Up to 50 nanometers per second

*Alisina Bazrafshan[1], Maria-Eleni Kyriazi[2], Brandon A. Holt[3], Wenxiao Deng[1], Selma Piranej[1], Hanquan Su[1], Yuesong Hu[1], Afaf H. El-Sagheer[4,5] and Tom Brown[4], Gabriel A. Kwong[3], Antonios G. Kanaras[2,6] and Khalid Salaita[1,3]**

[1] Department of Chemistry, Emory University, 1515 Dickey Drive, Atlanta, GA, 30322 USA,

[2] School of Physics and Astronomy, Faculty of Engineering and Physical Sciences, University of Southampton, Southampton, SO171BJ, UK

[3] *Wallace H. Coulter Department of Biomedical Engineering, Georgia Institute of Technology and Emory University, Atlanta, GA, 30322 USA*

[4] Department of Chemistry, University of Oxford, Chemistry Research Laboratory, 12 Mansfield Road, Oxford, OX1 3TA, UK

[5] Chemistry Branch, Department of Science and Mathematics, Faculty of Petroleum and Mining Engineering, Suez University, Suez, 43721, Egypt

[6] Institute for Life Sciences, University of Southampton, Southampton, SO171BJ, UK

**Correspondence to ksalaita@emory.edu*

ABSTRACT: synthetic motors that consume chemical energy to produce mechanical work offer potential applications in many fields that span from computing to drug delivery and diagnostics. Among

the various synthetic motors studied thus far, DNA-based machines offer the greatest programmability and have shown the ability to translocate micron-distances in an autonomous manner. DNA motors move by employing burnt-bridge Brownian ratchet mechanism, where the DNA "legs" hybridize and then destroy complementary nucleic acids immobilized on a surface. We have previously shown that highly multivalent DNA motors that roll offer improved performance compared to bipedal walkers. Here, we use DNA-gold nanoparticle conjugates to investigate and enhance DNA nanomotor performance. Specifically, we tune structural parameters such as DNA leg density, leg span, and nanoparticle anisotropy as well as buffer conditions to enhance motor performance. Both modeling and experiments demonstrate that increasing DNA leg density boosts the speed and processivity of motors, whereas DNA leg span increases processivity and directionality. By taking advantage of label-free imaging of nanomotors, we also uncover Lévy-type motion where motors exhibit bursts of translocation that are punctuated with transient stalling. Dimerized particles also demonstrate more ballistic trajectories confirming a rolling mechanism. Our work shows the fundamental properties that control DNA motor performance and demonstrates optimized motors that can travel multiple microns within minutes with speeds of up to 50 nm/s. The performance of these nanoscale motors approaches that of motor proteins that travel at speeds of 100-1000 nm/sec, and hence this work can be important in developing protocellular systems as well next generation sensors and diagnostics.

KEYWORDS. *synthetic DNA motors, gold nanoparticle, dynamic DNA nanotechnology, burnt bridge Brownian ratchet, spherical nucleic acids.*

Nanomachines are ubiquitous in nature.[1, 2] For example, the kinesin motors travel micron length distances on microtubules with nm/s velocities by hydrolyzing ATP.[3] Recapitulating the properties of these biological motors in synthetic systems has been a long-standing goal as these synthetic systems hold promise in the development of next generation sensors, molecular computers, and drug delivery platforms.[4-6]

In contrast to diffusional devices[7, 8] and nanoscale switches[9] that can toggle between isoenergetic states and can undo their own "work", nanoscale motors perform processive mechanical work. Commonly, nanomotors convert chemical energy into controlled nanomechanical motion through the burnt-bridge Brownian ratchet (BBR) mechanism. BBR is also harnessed by nature and is used to describe the enzymes involved in the partitioning of low copy number plasmids between daughter cells in bacteria.[10, 11] This mechanism involves binding of the motor to a "foothold" site, followed by a hydrolysis step that diminishes affinity to the occupied foothold, hence breaking symmetry and biasing motion to an adjacent unoccupied foothold site. The BBR mechanism is also chemically modular and has been shown to power nanomotors fueled through protein,[12] carbohydrate, [13] and nucleic acid chemical energy sources.

Amongst various BBR motors, DNA-based BBRs show great promise. This is because of the ability to tailor DNA into 3D structures with molecular precision using facile and highly accessible synthesis and self-assembly procedures. In addition, DNA hybridization and hydrolysis kinetics are highly tunable. The first demonstrations of DNA BBR motors had one or two legs. These motors could only undertake 1-5 consecutive steps (~10 nm).[14-17] Increasing the number of DNA legs leads to an increase in the processivity of DNA BBRs but at a cost of reduced speed.[18-20] This is due to the uncoordinated motion of individual DNA legs and points to a trade-off between polyvalency and speed. To increase the processivity of bipedal DNA walkers, Nir and coworkers used single molecule time-resolved FRET to reveal motor stepping dynamics and used this data to enhance motor design pushing the processivity from 7 to 32 consecutive steps with walking speed of 6 nm/hr. [21] In a separate study, Ellington and

coworkers increased the number of steps taken by a monoleg DNA walker[22] up to 38[23] and 47[24] steps/motor by increasing the number of legs[23] or introducing a cleat.[24]

Our group's efforts to create fast and efficient DNA BBR motors has focused on increasing the speed of multileg (polyvalent) DNA motors. The strategy has relied on powering these multileg BBR motors using RNase H, which has a high $k_{cat,}$ and engineering nano- and microscale structures that allow for rolling. [25, 26] Surreptitiously at first, and later by structure-functional analysis and modeling, we found that rolling overcomes the fundamental tradeoff between polyvalency and speed as it coordinates the motion of individual DNA legs. In our previous work, [27] we used DNA origami self-assembly[28] to generate the motor chassis and experimentally test structures that enable rolling of nanoscale motors. We found that rolling DNA origami nanomotors demonstrate unidirectional motion for ~μm distances within an hour.

Despite this progress, synthetic DNA BBR motors and even DNA-origami rolling motors remain ~one to two orders of magnitude slower than that of biological motors. Faster motors are desirable to foster the envisioned applications of nanoscale machines. Detailed investigations into the mechanism of chemical to mechanical energy conversion powering synthetic motors can optimize their efficiency, speed, and processivity.

Herein, we generate DNA motors with a gold nanoparticle "chassis" (DNA-AuNP). Organizing DNA legs around a gold particle chassis affords key advantages, which include the ability to generate high DNA leg density that would be very challenging to achieve using the origami technique[29] or using silica attachment chemistry.[30, 31] The thiol gold bond is a labile dative bond that allows for reconfiguration of DNA molecules to maximize packing density. Moreover, theoretical work by Schatz and colleagues suggests that the high local DNA density is accompanied by elevated local ionic strength and an enhanced collective on-rate of binding.[32] Another advantage of the AuNP chassis is that this scaffold provides a powerful label-free tag to visualize motor motions with high temporal (~50-500 msec) and spatial resolutions (~10 nm) without concern for photobleaching. Lastly, the past few decades of

nanoscience have generated facile procedures to synthesize and functionalize many different shapes and sizes of particles, and while not explored thoroughly in this work, it can be tested in principle to allow for mechanistic studies of motor mechanism. [33-38]

DNA-AuNP motors presented herein are processive for hours, can travel micron distances with speeds of multiple nanometers per sec which is an order of magnitude faster than DNA-origami motors and on par with some biological motors. We confirm that DNA-AuNP motors are efficient due to their ability to roll. Through a combination of experiments and modeling, we optimized the parameters of DNA leg density and span of DNA legs to enhance motor speed and processivity. By observing the motors with high time resolution, we discovered that DNA-AuNP motors display Levy-type motion, which shows bursts of speed followed by periods of slower motion. To our knowledge, DNA AuNP motors show the highest speed and greatest distances traveled for a nanoscale DNA-based motor to date.

Results and Discussion

Design and characterization of DNA-AuNP motors. A 3D illustration of our design is shown in **Figure 1a**. A gold nanoparticle is modified with DNA legs, which are complementary to a monolayer of single stranded RNA (ssRNA) immobilized on a glass slide (**Figure S1**). The ssRNA serves as the chemical fuel and is tagged with Cy3 to enable visualization of fuel consumption during BBR translocation (**Tables S1-S2**). **Figure 1b** highlights the reactions that drive BBR translocation of the motor. Briefly, the DNA legs hybridize to the complementary ssRNA fuel. This immobilizes the particle to the surface. Upon the addition of RNase H, RNA strands that are duplexed with the DNA legs are exclusively hydrolyzed, which frees the motor to hybridize to fresh ssRNA fuel sites. The net process of DNA leg hybridization, followed by RNA fuel consumption, and subsequent hybridization leads to a cycle that drives the motor to move forward away from consumed sites and toward untouched ssRNA fuel.

To facilitate detailed analysis of motor motion, we screened a range of nanoparticle sizes (**Figure S2-S4**) and found that 50 nm AuNPs (**Figure 1c, 1d)** were optimal offering high contrast in reflection interference contrast microscopy (RICM). These 50 nm AuNPs were functionalized with thiolated DNA

legs, as confirmed by UV-vis (**Figure S5**), and TEM (**Figure 1c**). To determine DNA leg density, the DNA was tagged with a FAM fluorophore (**Figure 1b**), and using a fluorescence calibration curve, the DNA density was found to be 1500 ± 150 molecules per particle (~1 DNA leg /5 nm^2 or 1.9 x 10^5 DNA leg/μm^2) (**Figure S6**). Importantly, this density is 7.2 times higher than the density of our previous DNA origami motors, which in principle, should lead to an enhancement in motor speed.

Introduction of DNA AuNP motors (~10 pM) to the RNA monolayer led to motor binding within minutes as observed by RICM (**Movie S1**). Widefield fluorescence microscopy showed bright FAM localizations of individual particles that colocalized with dark puncta observed in RICM (**Figure S2**, **Figure 1e** and **1f**). After washing the excess unbound particles, DNA-AuNP motors remained immobile due to DNA-RNA hybridization (**Movie S2**). Upon addition of RNase H, time-lapse RICM movies showed particle translocation across the surface (**Figure 1f**, **Movie S3**). Nanomotor motion colocalized with the loss of Cy3-tagged RNA fuel (**Figure 1e**,**1g**). We were able to localize the trajectory of the nanomotor based on the scattering of the gold particle motor observed using RICM (**Figure 1f**, **1h and Figure S7**). MSD analyses of this track showed an α coefficient of 1.6 (**Figure 1i**). MSD is proportional to time$^{\alpha}$, where α is a scaling factor that is 1 for random (Brownian) diffusion, < 1 for sub-diffusive motion, and > 1 (such as this trajectory) for super-diffusive motion.[39] Motors are also highly processive, as a plot of motor speed as a function of time shows that motion is maintained for ~hours (**Figure 1j**). Motor speed was maintained despite the slow dissociation of DNA legs (~30% loss in 1 hr) due to thiol-displacement reaction with 10 μM DTT in the buffer which is required for RNase H activity (**Figure S8, S9**). Note that the optimized conditions ([RNaseH], [formamide], [triton X]) used to conduct this experiment and the DNA leg sequence design (flexible polyT linker length and density) were the result of iterative screening and optimization of motor performance using single particle tracking (*vide infra*).

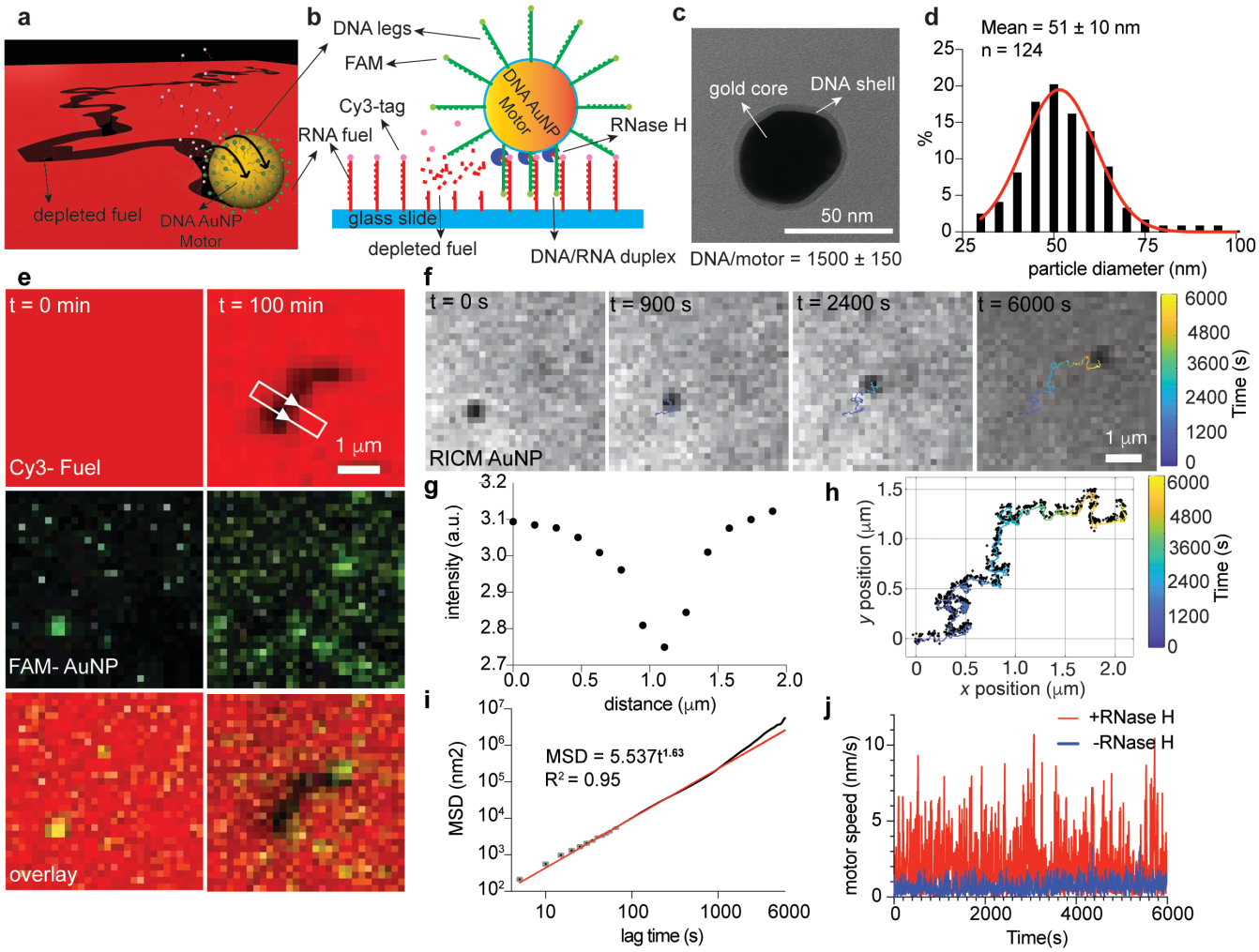

Figure 1. Design of DNA-AuNP nanoscale motors. (a) 3D illustration showing DNA-AuNP motor. (b) Side view scheme of motor highlighting the enzymatically driven mechanism of motion. RNase H specifically cleaves RNA hybridized to DNA legs but not single stranded RNA. (c) TEM image of 50 nm DNA AuNP motor stained with uranyl formate. (d) Histogram of DNA-AuNP diameters measured from TEM, *n* = 124 DNA-AuNP conjugates functionalized from two different batches. (e) Fluorescence images of FAM-AuNP and Cy3-fuel and overlay of a single DNA-AuNP motor at initial and final timepoints. (f) Timelapse RICM images of AuNP-motor. Colored line shows smoothed trajectory of a single motor obtained by finding the centroid from RICM time lapse. (g) Representative linescan profile of the region highlighted by white box in (e) demonstrating RNase H dependent hydrolysis of Cy3-RNA fuel. (h) AuNP motor RICM based localizations (black dots) with smoothed trajectory (colored line). Color indicates time from 0 to 6000 s (100 min). (i) Plot of MSD *vs* time for the same particle in (e) and (f). This plot is used to infer the α value for this

motor (α = 1.63). Black dots indicate average MSD for a given lag time, gray error bars represent the standard deviations of MSD for a given lag time. Red line shows the power fit to the data. (j) A plot of motor speed *vs* time for two motors with (same particle in (e), (h) and (i), red) and without (blue) RNase H.

Ensemble tracking shows that motors are fast and super diffusive. Using the MOSAIC localization software[40] along with smoothing[41] (**Figure S10)**, drift correction algorithms (**Figure S11**),[42] and custom MATLAB scripts we were able to analyze ensemble behavior of over 1000 motors at different conditions (**Figures S12-S14**). **Figure 2** shows a representative inverted RICM image offering motor locations (**Figure 2a**), Cy3-fuel depleted tracks (**Figure 2b**), overlay (**Figure 2c**) and the result of single particle tracking (**Figure 2d**). These localizations are color coded by time (0-30 min) and provide motor speed, net displacement and the duration of track attachment. **Figure 2e** (**left**) shows n = 86 trajectories overlaid with the origin as the start position. Trajectory lengths were negligible when RNase H was withheld (**Figure 2e, right**), which confirms the role of RNase H in driving motion of these particles as well as the quality of our particle tracking algorithms. Histograms plotting motor speeds of hundreds of tracks show that motors can reach 10 nm/s with an average of 3.0 ± 1.7 nm/s (**Figure 2f**). This value is on par with the speed of biological motor proteins.[1, 43] Furthermore, analyses of 280 motors confirmed that most tracked particles (85%) were super diffusive with an average α = 1.37 (**Figure 2g**). A recent modeling study showed that in systems where motors progressively dissociate from the surface, selecting only the track-bound BBRs for analysis can lead to bias and an over-estimate of α.[44] However, in our system, we observed that a subset of motors tend to stall as well as dissociate over longer observation times. Careful analysis of α confirmed that most motors are super-diffusive throughout the 30 min acquisition and there is no over-estimate bias of α (**Figure S13** and **S15**).

Optimizing enzyme concentration and buffer conditions. We investigated the role of RNaseH concentration and buffer in tuning motor performance. **Figure 2h** shows the effect of enzyme concentration on net displacements. This experiment revealed that net displacement increased with

increasing RNaseH concentrations up to 30 nM. Greater concentrations of RNase H did not further boost the average net displacement of motors. Motor speed is limited by enzyme concentration in the regime of low [RNaseH]. At greater [RNaseH], net displacement saturates, suggesting that the rate limiting step is no longer the k_{cat} *i.e.,* the rate of RNA hydrolysis. Despite having different net displacements, most motors were super diffusive ($\alpha>1$) in all conditions with RNase H present. (**Figure 2i**).

Interestingly, enzyme concentrations also tune motor processivity as higher concentrations lead to more rapid surface dissociation (25% more motor dissociation at t =10 min as RNase H increased from 30 to 240 nM) (**Figure 2j** and **2k**). Modelling of DNA BBRs using a Monte-Carlo & Gillespie algorithm also shows that motor speed increases with enzyme concentration up to a certain threshold (**Supplementary Materials and Methods - K**, **Figure S16**). In the model, increasing enzyme concentration decreases the attachment time of particles, as more enzyme increases the probability of all DNA legs simultaneously occupying the unbound state. Accordingly, we proceeded with the 30 nM enzyme concentration for the remainder of this study. We subsequently tested the role of denaturant (formamide) and surfactant (triton X) in tuning motor performance. In the presence of both formamide and triton, motors generate twice the net displacement compared to a solution that includes either formamide or triton X only in the 1X RNase H buffer (**Figure 2l**). Regardless of the variations in net displacement, motors remain super diffusive in the presence of these additives (**Figure 2m**). Quantifying the fraction of motors that remain bound as a function of time showed that denaturant and surfactant (at the concentrations tested) have no significant effect on motor processivity (**Figure 2n**, **2o**). These experiments show how optimizing buffer conditions can significantly boost motor performance.

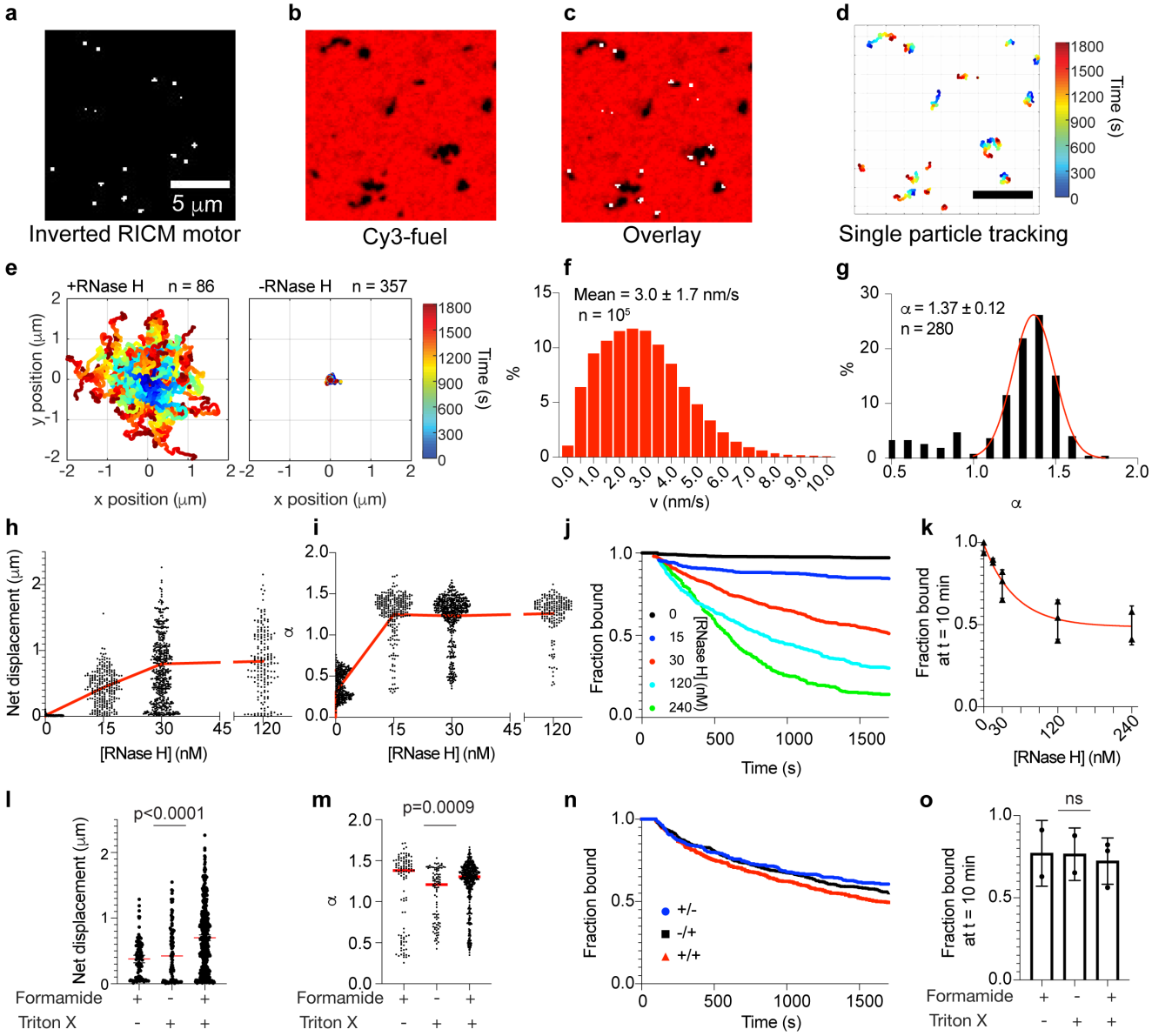

Figure 2. Ensemble tracking of motor behavior. (a) Inverted RICM showing the location of DNA-AuNP motors. (b) Cy3 channel image showing fuel depleted tracks. (c) Overlay of inverted RICM and Cy3 image showing colocalization and loss of fuel in wake of motor. (d) Single particle trajectories from a `30 min timelapse RICM movie from region highlighted (a)-(c). (e) Ensemble motor trajectories plotted from the center of coordinates (0,0) with 30 nM RNase H (left, *n* = 86) and without RNase H (right, *n* = 357). Color indicates time from 0 to 30 min. (f) Histogram of motor speed generated from 10^5 data points from hundreds of motors from 3 independent experiments. The histogram mean and standard deviation is calculated from the raw data. (g) Ensemble α values of motors demonstrating self-avoiding behavior. 85% of the motors have α>1.

A Gaussian fit to $\alpha>1$ shows $\alpha = 1.37 \pm 0.12$ for super-diffusive motors in the presence of 30 nM RNase H. (h) Plot of net displacements and (i) α values for motors as a function of [RNaseH]. Each dot represents a single motor. The red line connects the means of each sample. *n* = 300, 218, 340 and 148 motors for 0, 15, 30 and 120 nM concentrations, respectively, generated from 3 independent experiments. (j) Plot of fraction of motors bound to surface as a function of time for motors with different [RNaseH] (same trajectories from (i)) and (k) plot of fraction of motors bound at *t*=10 min. Error bars represent the standard deviation from three (0, 15, 30, 120 nM RNase H) or two (240 nM RNaseH) independent experiments. (l) Plot of net displacements and (m) α values as a function of formamide/triton X addition. Each dot represents a single motor. The red line indicates the means of each sample. *n* = 103, 97 and 156 for +/-, -/+ and +/+ conditions, respectively. ANOVA summary *p* values for each plot are indicated above. (n) Plot of fraction of motors bound to surface as a function of formamide and triton X. (o) Plot of fraction of motors bound at *t*=10 minutes. Error bars represent the standard deviation from three (+/+) or two (+/- and -/+) independent experiments.

Increasing DNA leg density boosts motor speed and processivity. Previous modeling by Forde and colleagues along with our experiments using DNA origami nanostructures suggested that increasing DNA leg density enhances motor speed.[45] The relationship between track attachment time (motor processivity) and DNA leg density is more complex, with two recent papers by Forde and colleagues suggesting that the relationship depends on the affinity between the DNA legs and the consumed fuel site.[20, 45] Our model (**Figure S17**), in agreement with Forde *et al.*, predicts increasing density of DNA legs will lead to increased processivity because of the affinity between DNA legs and partially hydrolyzed fuel sites.

To test these predictions, we generated a library of motors modified with a binary mixture of two DNA strands- keeping the total thiol-DNA concentration constant- one that was the DNA leg and the second as a non-specific DNA oligo (poly T). The advantage of this approach is that motor charge density and

its chemical environment was maintained (**Figure 3a**). We quantified DNA leg density on each motor by gold dissolution and comparing FAM-DNA fluorescence to that of a calibration standard. The library of AuNP motors had DNA leg densities ranging from 1.25 x 10^5 to 1.90 x 10^5 DNA legs/μm^2 (**Figure 3b and Figure S18**). Across these DNA leg densities, all motors were functional and translocated on the complementary RNA chips (**Figure 3c**). Measurement of the fraction of particles remaining bound to the surface as a function of time after RNaseH addition showed that increasing DNA leg density led to a slight increase in processivity (**Figure 3d**). For example, 75± 9% of the highest DNA density motors (1.90 x 10^5 DNA legs/μm^2) remained bound at t=10 min after initiating motion, while only 56 ± 5% of the low-density motors (1.25 x 10^5 DNA legs/μm^2) remained bound at the same time point (**Figure 3e**). By selecting the motors that remained processive for the duration of the 30 min video, we observed an increase in net displacement with increasing DNA leg density (**Figure 3f**). This increase in total displacement was accompanied with an increase in number of motors being super diffusive in the course of 30 minutes ($\alpha > 1$, **Figure 3g**) as well as an increase in motor speed (**Figure 3h**).

This experimental result confirms the prediction that increasing leg density leads to a counter-intuitive increase in motor speed (**Figure S17**). If viewed from the perspective of the DNA motor, a greater DNA leg density requires more catalytic turnovers to move the particle a set distance. However, if viewed from the perspective of the RNA monolayer, particle motion requires removal of a critical density of RNA to facilitate motion. Greater DNA leg density allows for parallel cleavage events to occur, and thus allowing the particle to move faster. These data show that increasing DNA leg density enhances the rate of RNA hydrolysis (by effectively increasing the concentration of enzyme-substrate (E-S) complex). In addition, increasing leg density is also advantageous as it leads to improved processivity by reducing the probability of spontaneous dissociation from the track or stalling.

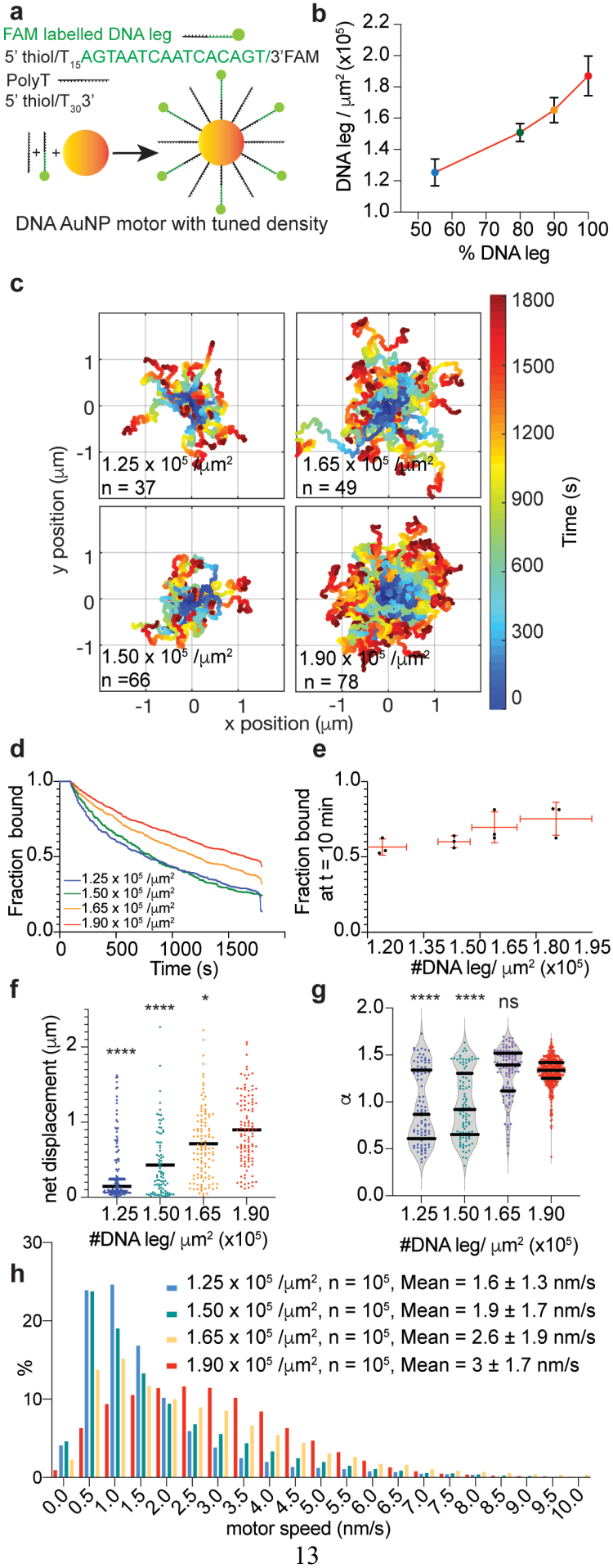
a
FAM labelled DNA leg
5' thiol/T15AGTAATCAATCACAGT/3'FAM
PolyT
5' thiol/T30 3'
DNA AuNP motor with tuned density
b
DNA leg / μm² (x10⁵)
% DNA leg
c
1.25 x 10⁵ /μm²
n = 37
1.65 x 10⁵ /μm²
n = 49
1.50 x 10⁵ /μm²
n =66
1.90 x 10⁵ /μm²
n = 78
y position (μm)
x position (μm)
Time (s)
d
Fraction bound
Time (s)
1.25 x 10⁵ /μm²
1.50 x 10⁵ /μm²
1.65 x 10⁵ /μm²
1.90 x 10⁵ /μm²
e
Fraction bound at t = 10 min
#DNA leg/ μm² (x10⁵)
f
net displacement (μm)
#DNA leg/ μm² (x10⁵)
g
α
#DNA leg/ μm² (x10⁵)
h
1.25 x 10⁵ /μm², n = 10⁵, Mean = 1.6 ± 1.3 nm/s
1.50 x 10⁵ /μm², n = 10⁵, Mean = 1.9 ± 1.7 nm/s
1.65 x 10⁵ /μm², n = 10⁵, Mean = 2.6 ± 1.9 nm/s
1.90 x 10⁵ /μm², n = 10⁵, Mean = 3 ± 1.7 nm/s
%
motor speed (nm/s)

Figure 3. Effect of DNA leg density on motor motion. (a) Schematic used to tune the density of DNA legs on 50 nm DNA gold particles. (b) Plot of density of DNA legs/μm^2 as a function of %DNA leg in DNA solution for AuNP functionalization. (c) Trajectories of motors with different DNA leg density with color indicating time from 0 to 30 min. (d) Plot of fraction of motors bound to surface as a function of time for motors with different DNA leg density and (e) plot of fraction of motors bound at t=10 minutes. Vertical and horizontal error bars represent the standard deviation for 3 independent experiments. (f) Plot of motor net displacement and (g) α value as a function of DNA leg density. Each dot represents a single motor while the horizontal line represents the mean from (*n*= 99, 89, 114 and 121 for 1.25 x 10^5, 1.5 x 10^5, 1.65 x 10^5 and 1.90 x 10^5 DNA leg/μm^2 samples, respectively generated from 3 independent experiments). **, * and ns indicate that p<0.0001 and p = 0.019 and not statistically different when compared to 1.90 x 10^5 DNA leg/μm^2 density group. Horizontal black lines in (g) represent the median and quartiles of the distribution of α values. (h) Histograms of motor speeds for motors with different DNA leg density. Each histogram is comprised of 10^5 motor speed data points generated from trajectories of 3 independent experiments characterized in (d)-(g). The histogram mean and standard deviation is calculated from the raw data.**

DNA leg span increases motor processivity. DNA leg "span" is defined as the number of RNA fuel sites that are accessible to a given DNA leg. We modeled how span impacts motor performance using our Monte-Carlo and Gillespie algorithm (**Figure S18**). In our model, span was tuned by increasing the effective particle size while maintaining the same polyvalency, and increasing this parameter led to a significant enhancement in processivity (**Figure S18**). To experimentally test the role of DNA leg span, we generated AuNP with DNA legs linked to the motor chassis using a T3, T15, T30, and PEG18-T15 spacer (**Figure 4a)**. Increasing the length of the T spacer in the DNA legs led to a decrease in surface density, as would be expected based on prior work (**Figure 4b, Figure S18).**[46] As an additional variant, we introduced a PEG linker (PEG18) since this maintains DNA density while providing additional span

(**Figure S18**). By analyzing tens of trajectories from each type of motor (**Figure 4c)**, we found that motors with higher span were more processive (**Figure 4d, 5e**), and traveled greater distances (**Figure 5f**). Almost half of the T3 motors bound to the surface demonstrate a low α value due to premature stalling and greater spans also allowed for a slight increase in the α value (**Figure 4g**). These effects were more pronounced for the PEG18-T15 DNA legs since DNA leg density was maintained at a level similar to the T15 for this group. Despite the 20% reduction in DNA density for T30 DNA legs group, the increase in leg span outweighed the effect of reduced DNA leg density and generated greater processivity. The model explains these experimental results by predicting that increasing DNA span improves processivity by increasing the probability of foothold binding (**Figure S19**). Our results in studying the effect of span are in agreement with previous modelling that increasing span leads to increase in track attachment time.[45] However, we did not see a decrease in α in the conditions tested through experiments and modelling; modelling by Forde et. al predicts that α will decrease with increasing span.[45] This prediction may hold if we increased span to distances of ~50-100 nm which is comparable to the particle size.

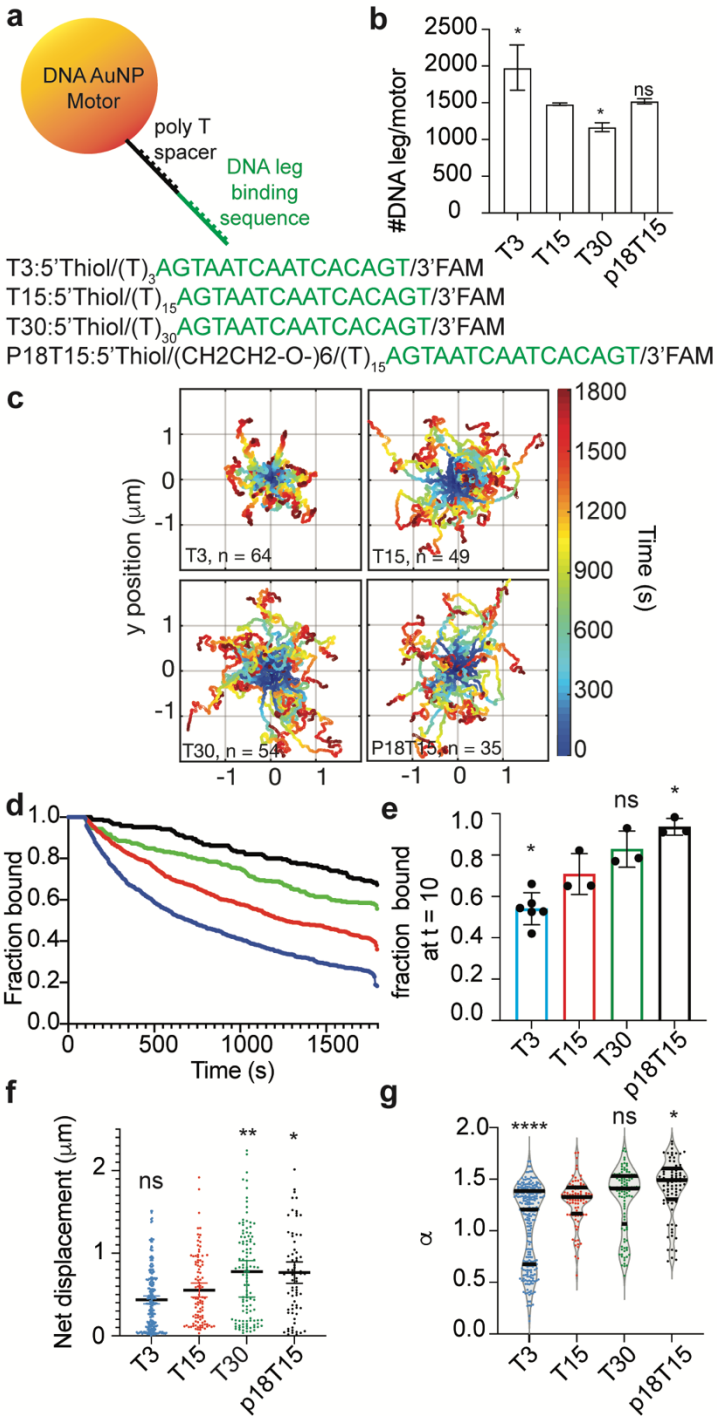

Figure 4. Effect of DNA leg span on AuNP motor motion. (a) Schematic showing how DNA leg span was tuned using sequences with varying lengths of T spacers and PEG. (b) Plot of DNA copy number per motor for different DNA legs. * indicates $p = 0.019$ (T3 *vs* T15), and $p = 0.029$ (T30 *vs* T15) and ns indicates not statistically different (P18T15 *vs* T15). (c) Trajectories of motors with different DNA leg span with color indicating time from 0 to 30 min. (d) Plot of fraction of motors bound to surface as a function of time and (e) plot of fraction of motors bound at t=10 minutes. *

and ns indicate p = 0.049 (T15 *vs* T3), 0.020 (T15 *vs* p18T15) and not statistically different, respectively. Each dot represents one replicate and the error bars indicate the standard deviation. (f) Plot of motor net displacement and (g) α value as a function of DNA leg span. Here, each dot represents a single motor while the horizontal line represents the mean from (n= 257, 99, 115 and 73 for T3, T15, T30 and P18T15 samples, respectively). The data for each DNA span category was pooled from three independent experiments, with the exception of the T3 which was pooled from six independent experiments. **, * and ns in (f) indicate that p=0.002 (T15 *vs* T30), p = 0.019 (T15 *vs* p18 T15) and not statistically different (T3 *vs* T15). Horizontal black lines in (g) represent the median and quartiles of the distribution of α values. **, * and ns indicate p<0.0001, p = 0.038 and not statistically different when compared to T15 group.**

High-temporal resolution particle tracking shows Lévy-type motion in AuNP motors. An interesting observation in the trajectories generated by our simulation algorithm was that motors travelled in bursts of motion followed by slower diffusion (**Figure S20**). Taking advantage of label-free particle tracking with RICM, we are able to acquire time-lapse movies showing the motion of 50 nm AuNP motors with a frame rate as rapid as 2 Hz. This number of localizations is not possible when using fluorescence microscopy because of the limited photon budget when employing conventional dyes. A control experiment using stalled motors showed that increasing the frame rate to 2 Hz had minimal effect on localization precision (**Figure S21)**. Thus far, all imaging was performed at 0.2 Hz frame rate, and this showed that particles moved continuously (**Figure 2g, Figure 5a**). However, when tracking motors at 2 Hz, we discovered that their motion was not continuous. Rather, motors displayed intervals or bursts with large steps (15-35 nm) alongside periods of moving with small steps (2-5 nm) (**Figure 5b, S22)**. This is better represented by the distribution of individual steps (d, distance between two consecutive time points). When motors are tracked at 0.2 Hz frame rate, almost all observed values of d (and accordingly motor speed in **figure 2j**) are higher than the background noise, suggesting motor motion is continuous. However, when motors are tracked with the 2 Hz frame rate, 50% of the observed

values of *d* are comparable with background noise and the distribution of *d* shows a heavy tailed distribution (**Figure 5c, S22**). Heavy tailed probability distributions of steps are known as Lévy walks or Lévy type motion which have been used to characterize the motion of marine vertebrates,[47] birds,[48] T cells[49] and even swarming *E. coli.*[50] Mathematically, Lévy-walks are drawn from a probability distribution with a power-law tail where P(*d*) of the tail is distributed as a function of step size (*d*) to the power of -μ. When $1 < \mu \leq 3$, the motion is characterized as a Lévy walk.[47, 48, 50] When analyzing the trajectory in **Figure 5b**, we found that the motor showed $\mu = 2.8$. Ensemble analyses of nanomotor trajectories from $n = 33$ particles with [RNase H] = 30 nM exhibited a Lévy-type motion with $\mu = 2.4 \pm 0.3$ for the population. Interestingly, we found that simulated particles exhibited $\mu = 2.5 \pm 0.2$ which is similar to our measured values (**Figure 5f**). Analyses of step sizes on motors with different DNA leg densities revealed that μ decreases with increasing DNA density (**Figure 5g**). This result suggests that motors with greater DNA leg density display a higher probability of taking longer steps (**Figure S23**). This experimental finding is consistent with our observation that increasing DNA leg density enhances motor performance (processivity and speed) (**Figure 3**). Our model shows a similar trend (**Figure 5g),** and indicates that at higher DNA leg densities, large steps are driven by transient stalling of the motor until all proximal fuel sites are consumed, thus freeing the motor to take a step that can be as large as one body length (~50 nm). Conversely, lower leg density reduces the probability of taking such large steps.

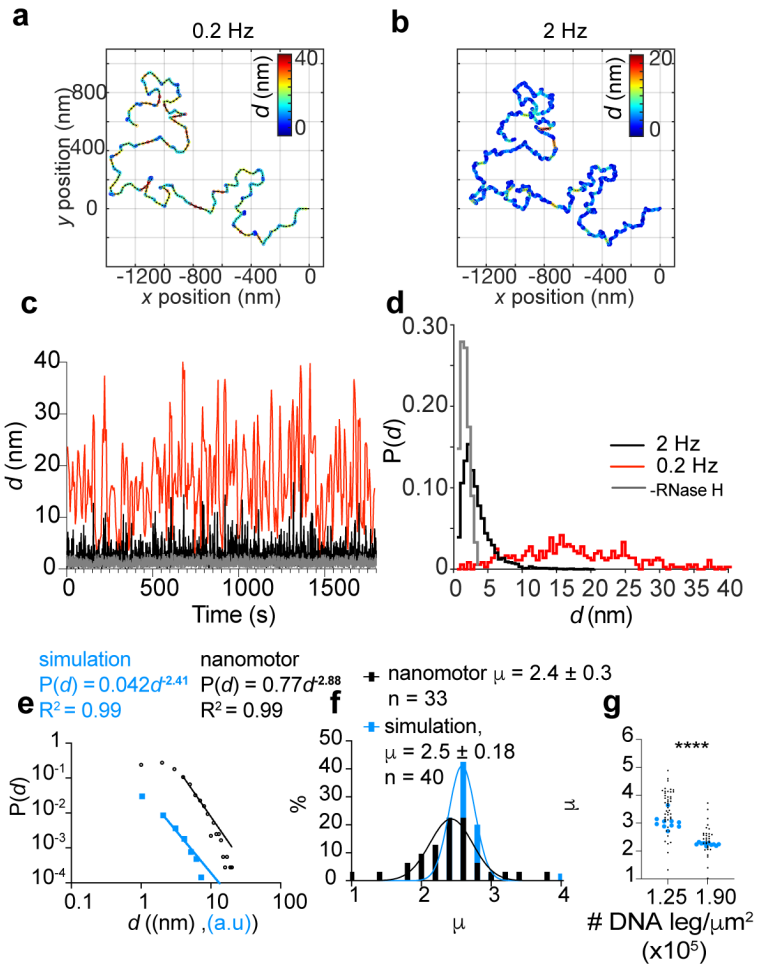

Figure 5. Motors display Lévy type motion. Representative experimental motor trajectory for the same motor tracked at (a) 0.2 and (b) 2 Hz imaging rates. Trajectories are color coded by the size of the individual step (*d*) between two consecutive time points. (c) Plot of individual step size (*d*) *vs* time for an individual motor tracked at 0.2 (red) and 2 Hz (black) imaging rates and the step sizes of a motor tracked at 2Hz in the absence of RNaseH (noise, gray). (d) Probability density function of step size (*d*) for different imaging rates shows different distributions depending on imaging rate. (e) The heavy tail of the probability distribution for step size of simulated (blue) and experimental (black) tracks show Lévy type motion. (f) Histograms of Levy coefficients (μ) for nanomotor experiments (black) and simulations (blue). Lines show Gaussian fits to the histograms from which the mean and standard deviations are extracted. (g) Increase in Lévy coefficient (μ) with decreasing density of DNA legs. ** shows $p < 0.0001$. Each black dot represents the Levy**

coefficient of a nanomotor while each blue dot shows the Levy exponent for a simulated trajectory.

Motors travel *via* a rolling mechanism. Previous work showed that polyvalent *rolling* micromotors[25] and nanomotors[27] with an anisotropic chassis can roll unidirectionally. To test if gold nanoparticle motors move by rolling, we aimed to generate an anisotropic motor chassis. One approach to engineer such anisotropic DNA-AuNP motors is by dimerizing the motors using hybridization-driven click chemistry.[35] A schematic of this approach is shown in **Figure 6a**. The rationale was that dimers of particles would function as two "wheels" linked through 24-mer double stranded DNA and hence would display more linear trajectories compared to the monomeric particles. TEM and UV-vis analyses of dimerized particles confirmed dimerization of the structure (**Figure 6b, S24**). Quantitative TEM analyses of hundreds of nanoparticles showed that ~30% of AuNPs were dimerized, with the remaining particles primarily as monomers (**Figure S24**). The yield was relatively low compared to reported yields for smaller sized particles due to the challenges of purifying dimerized 50 nm AuNP *via* gel electrophoresis.[51] Upon addition of RNase H, we imaged the motors in the RICM and FAM channels and observed the depletion tracks using the Cy3 channel (**Figure 6c**). Analysis of the Cy3 depletion tracks revealed that a subset of the trajectories displayed a linear component with some motors traveling ballistically over multiple microns (**Figure 6c**, **Figure S25, S26**). To quantify track linearity, we measured the motor Kuhn segment length from the RICM trajectories (**Figure 6d**). Analyses of Kuhn segment lengths for populations of motors showed that in the dimer samples, 25% of the motors showed trajectories with a Kuhn segment length > 250 nm. This sub-population is minimal for the monomer nanoparticle motors and likely the result of AuNPs with high aspect ratio (**Figure 6e, Figure S5d**), which supports rolling as a mechanism of translocation.

We next analyzed the Cy3 depletion track widths as this metric provides additional evidence to the rolling mechanism, as dimer motors that roll should display a track width that matches the span of the DNA legs. Geometric modelling of dimers suggests that the dimers can span between 125 - 175 nm (**Figure S27**). Taking advantage of the enriched population of linear tracks, we used Structured

Illumination Microscopy (SIM) to quantify track widths. Analyses of Cy3-depleted tracks showed trackwidths ranging from 150-350 nm. Given the variation in particle size and noise of SIM measurement and the fact that the minimum track width was ~150 nm, the data is consistent with a rolling mechanism (**Figure S28**).

As an additional control we blocked the remaining vacant DNA leg sites on monomeric DNA-AuNP motors after hybridizing to the RNA surface. In this experiment, we observed that blocked motors did not move and dissociated rapidly (**Figure S29**). Taken together, these multiple lines of evidence strongly support that AuNP motors primarily move through a rolling mechanism.

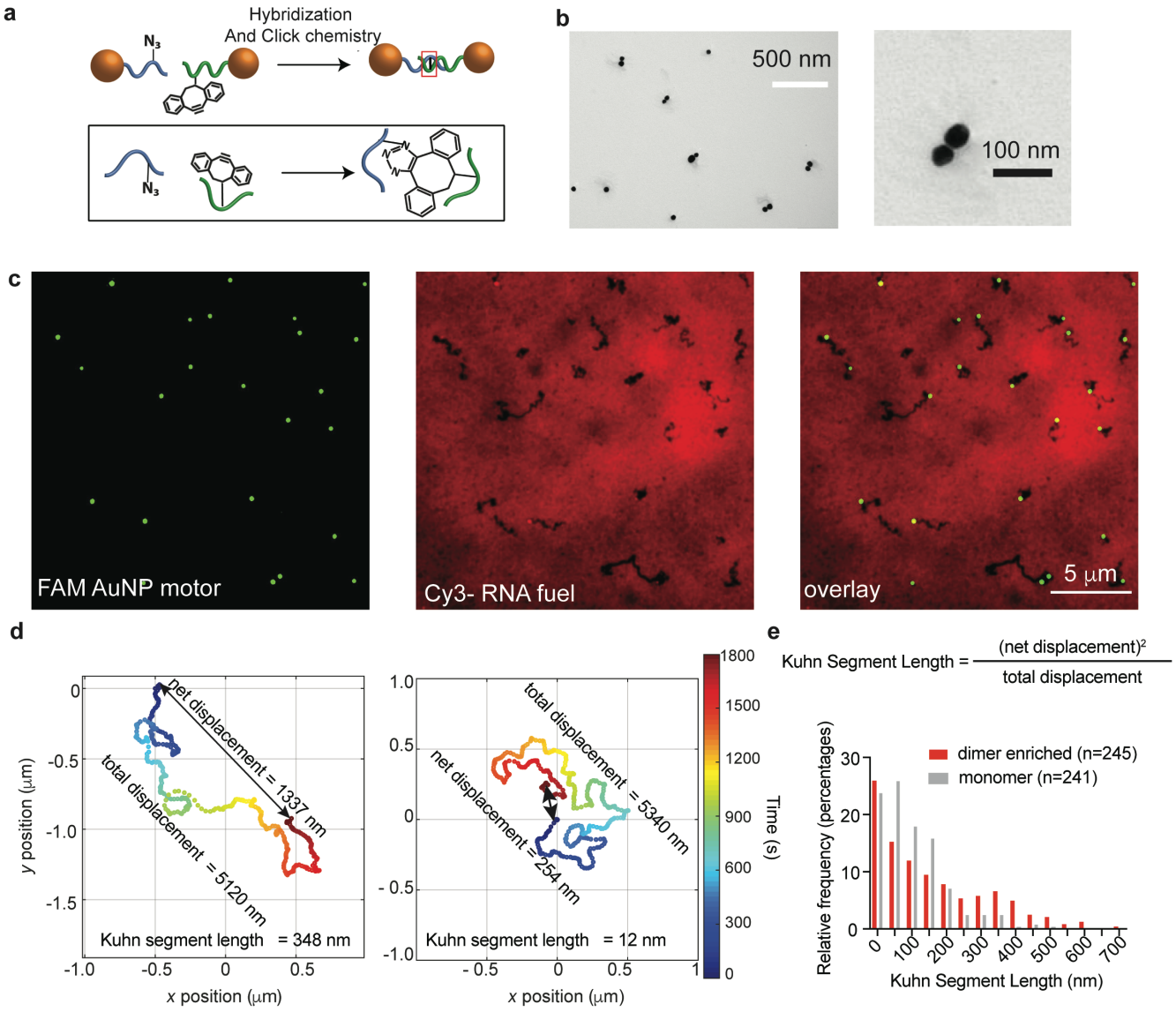

Figure 6. Anisotropic DNA-AuNP motors confirm a rolling mechanism of motion. (a) Schematic showing the approach used to form chemically ligated DNA 50 nm gold nanoparticles utilizing copper free click chemistry. (b) TEM of dimerized sample highlighting a region of the grid with multiple examples of dimerized particles. Zoom-in shows a single dimer. (c) Representative SIM images (FAM, Cy3 and overlay) of FAM-labeled AuNP motors that were allowed to translocate for 1 hr. (d) Two representative trajectories highlighting different Kuhn segment values with color indicating time from 0 to 30 min. Data was obtained using RICM time lapse tracking as described in methods section. (e) A histogram of Kuhn segment lengths for 3 runs from two particle batches. One batch was synthesized as monomeric AuNP motors (grey) while the second batch contained 30% dimer AuNP (red). Note that dimer enriched sample shows a population of trajectories with high (>250 nm) Kuhn segment lengths.

Conclusion

To the best of our knowledge, this work shows the fastest and most processive DNA nanomotor reported to date. By optimizing buffer and enzyme concentration, as well as DNA leg density and span, we have created a DNA nanomotor that can travel micron length distances within minutes, with bursts of speed reaching 50-70 nm/s. The label-free scattering-based imaging of 50 nm gold particle motors allows for tracking at high time and spatial resolution. By imaging at high time resolution, we discovered that motors display Lévy type motion, where the motors show bursts of high speed punctuated by brief stalling periods in between. We also uncover the fundamental principles that may further boost speed, as increasing DNA leg density leads to a higher probability of larger steps.

Anisotropic shaped motors validate that motors primarily move by rolling. The data also strongly suggests that efficient motor performance is mediated and enhanced by motor rolling as blocking the rolling mechanism leads to minimal translocation and rapid motor dissociation. In closing, we note that gold nanoparticle motors now achieve speed and processivity that approaches that of biological motor proteins that move on a track with ~100-1000 nm/sec speeds to move cargo in cells and drive locomotion of animals. Our work lays the foundation of how to further improve the performance of synthetic motors and given the programmability of DNA machines one can envision future applications in sensing, drug delivery and diagnostics.

MATERIALS AND METHODS

All chemicals were purchased from Sigma-Aldrich unless otherwise noted. Stock solutions were made using Nanopure water (Barnstead™ Nanopure™ system, resistivity = 18.2 MΩ, Thermofisher, Waltham, MA), herein referred to as DI water. Oligonucleotides were custom synthesized by Integrated DNA Technologies (Coralville, IA) and are summarized in Tables S1. RNase H was obtained from Takara Clontech (Product No. 2150A). All motor translocation measurements were performed in IBIDI (Fitchburg, WI) sticky-Slide VI 0.4 channels (Product No. 80608) or in custom made Delrin chambers. Delrin ¼"x 12" x 12" Sheet (Product No. 8573K15) and 2-sided Optically Clear Mounting Tape (Product No. 7602A53) were purchased from McMasterCarr (Douglasville, GA). Azido-PEG4-NHS ester was purchased from Click Chemistry Tools (Scottsdale, AZ, Product No. AZ103-1000).

Synthesis of monomer motors (50 nm DNA-AuNP conjugates)

Modification of 50 nm gold nanoparticles with thiolated DNA was achieved using a recently published method [52]. Briefly, 20 μL of 100 μM thiolated DNA was added to were added to 180 μL of a solution of commercially purchased 50 nm diameter gold nanoparticles from Sigma-

Aldrich (Cat # 753645) in DI water in a glass vial. The solution was cooled and frozen by placing it in a –30 °C freezer for 15 min. Subsequently, the 200 μL solution was allowed to thaw at room temperature for 30 min. Freeze-thaw cycles were repeated three times. Then, in order to remove unbound thiolated DNA legs, the solution was centrifuged (5000 rpm for 8 min) and washed with 1 mL of 1X PBS seven times. The resulting modified DNA-AuNPs were stored at 4 °C and used within one week after synthesis. Detailed methods of tuning leg density, preparation of dimer particles, quantification of the number of DNA legs per motor and TEM acquisition of motors can be found in supplementary materials and methods.

RNA monolayer preparation

RNA monolayer preparation was performed following previously published protocols.[27] For details see supplementary materials and methods and Figure S1.

Optical microscopy

A Nikon Ti Eclipse microscope was used for all widefield imaging of nanomotors. The microscope was equipped with an Intensilight epifluorescence source (Nikon), a CFI Apo 100x NA 1.49 objective (Nikon). The microscope also included a Nikon Perfect Focus System, which allows the capture of multipoint and time-lapse images without loss of focus. FITC and Cy3 images were obtained using the Quad Cube (Product No. 97327) and TRITC (Product No. 96321) filter cube set supplied by Chroma. For time lapse experiments, using the ND acquisition toolbox in the Elements software package, one RICM image with 500 ms exposure time was captured every 5 seconds for 0.2 Hz frame rate. For 2 Hz frame rate, one RICM image with 500 ms exposure time was captured every 500 ms (continuous imaging using the “fast time lapse” add-on). The images were collected at 16-bit depth using an Andor EMCCD iXON DU897 512x512 camera. All imaging was conducted at room temperature.

A Nikon Ti2 microscope was used to capture wide field fluorescence images of depletion tracks after the time lapse to quantify percent fluorescence loss during motor motion and Kuhn segment analyses. This microscope was equipped with SOLA SE Light Engine. and Nikon Perfect Focus System. The images were collected at 16-bit depth using Prime 95B 25mm™ Scientific CMOS 1608x1608 Camera (Photometrix, AZ). Methods for RICM tracking of 50 nm motors, analyses of trajectories and computational modelling of DNA motors are described in supplementary materials and methods.

Super-resolution imaging (SIM) of the fluorescence-depletion tracks

SIM images were acquired on a Nikon N-SIM system equipped with a CFI Apo 100x 1.49NA objective and an Andor iXon EMCCD (60 nm per pixel). For each N-SIM image, nine images of a 3′-Cy3-RNA sample were acquired in different phases using a 561 nm laser as an excitation source and were reconstructed using the Nikon Elements software package.

ASSOCIATED CONTENT

Supporting Information

The Supporting Information is available free of charge on the ACS Publications website.

Materials and Methods, supplementary data and analyses, (Supplementary Material.pdf)

Supplementary Movies:

Movie S1: A representative time lapse video of DNA-AuNP motors binding to an RNA surface. Imaging was initiated after adding a 10 pM solution of DNA-AuNP motors in 1X RNase H buffer to the RNA surface. The images were acquired using a 100x 1.49 NA objective at a frequency of 1 Hz. Note that individual DNA coated nanoparticles are observed as dark puncta. Scale bar = 10 μm. (movie_S1.mp4)

Movie S2: A representative time lapse video of DNA-AuNP motors in the absence of RNase H. Particles are completely immobile due to RNA/DNA hybridization. Imaging was initiated after adding 100 uL of buffer containing 10% (v/v) formamide, 0.75% (v/v) triton X and 1X RNase H buffer. The images were acquired using a 100x 1.49 NA objective at a frequency of 0.2 Hz for 30 minutes. Scale bar is 10 μm. (movie S2.mp4)

Movie S3: A representative time lapse video of DNA-AuNP motors in the presence of RNase H. Particles roll along the surface. Imaging was initiated after adding 100 uL of buffer containing 10% (v/v) formamide, 0.75% (v/v) triton X, 1X RNase H buffer and 30 nM of RNase H. The images were acquired using a 100x 1.49 NA objective at a frequency of 0.2 Hz for 30 minutes. Scale bar is 10 μm. (movie S3.mp4)

The authors declare no competing financial interest.

AUTHOR INFORMATION

Corresponding Author

* Khalid Salaita, PhD
Email: k.salaita@emory.edu

ORCID:
Alisina Bazrafshan: 0000-0002-3259-8196
Maria-Eleni Kyriazi
Brandon Holt
Wenxiao Deng
Selma Piranej
Hanquan Su: 0000-0002-5029-580X
Yuesong Hu
Afaf H. El-Sagheer: 0000-0001-8706-1292
Tom Brown: 0000-0002-6538-3036
Gabriel A. Kwong: 0000-0002-6255-6755
Antonios G. Kanaras: 0000-0002-9847-6706
Khalid Salaita: 0000-0003-4138-3477

Author Contributions

A.B. and K.S conceived of the project. A.B designed and performed most of the experiments. M.K and A.G.K provided AuNP dimers and monomers. B.A.H helped with modelling of AuNP motors. W.D helped with trajectory analyses. Y.H helped with experiments measuring density of DNA on AuNP motors. All authors participated in discussions and revision of the paper. A.B and K.S wrote the manuscript.

ACKNOWLEDGMENT

We thank Armina Fani for her artwork demonstrating the Scheme in Figure 1a and the TOC figure. We thank Dr. Justin Burton for providing access to use the laser cutter in his lab. Furthermore, we acknowledge support from Robert P. Apkarian Integrated Electron Microscopy Core and Emory University Integrated Cellular Imaging Microscopy Core. We thank Dr. Guram Gogia (Guga) for insightful conversations that led us to the literature and physical principles of Lévy flights. We acknowledge support from **NSF DMR 1905947**, **NIH R01 GM124472**, and **NSF- CHE 2004126.**

REFERENCES

1. Sato, O.; Komatsu, S.; Sakai, T.; Tsukasaki, Y.; Tanaka, R.; Mizutani, T.; Watanabe, T. M.; Ikebe, R.; Ikebe, M., Human Myosin VIIa Is a Very Slow Processive Motor Protein on Various Cellular Actin Structures. *J Biol Chem* **2017,** *292* (26), 10950-10960.
2. Yildiz, A.; Forkey, J. N.; McKinney, S. A.; Ha, T.; Goldman, Y. E.; Selvin, P. R., Myosin V Walks Hand-Over-Hand: Single Fluorophore Imaging with 1.5-nm Localization. *Science* **2003,** *300* (5628), 2061.
3. Vale, R. D.; Funatsu, T.; Pierce, D. W.; Romberg, L.; Harada, Y.; Yanagida, T., Direct Observation of Single Kinesin Molecules Moving along Microtubules. *Nature* **2019,** *380* (6573), 451.
4. Shao, J.; Cao, S.; Williams, D. S.; Abdelmohsen, L. K. E. A.; van Hest, J. C. M., Photoactivated Polymersome Nanomotors: Traversing Biological Barriers. *Angewandte Chemie International Edition* **2020,** *59,* 16918.
5. von Delius, M.; Leigh, D. A., Walking Molecules. *Chem Soc Rev* **2011,** *40* (7), 3656-76.
6. Valero, J.; Škugor, M., Mechanisms, Methods of Tracking and Applications of DNA Walkers: A Review. *ChemPhysChem* **2020,** *21* (17), 1971-1988.
7. Li, J.; Johnson-Buck, A.; Yang, Y. R.; Shih, W. M.; Yan, H.; Walter, N. G., Exploring the Speed Limit of Toehold Exchange with a Cartwheeling DNA Acrobat. *Nature Nanotechnology* **2018,** *13* (8), 723-729.
8. Thubagere, A. J.; Li, W.; Johnson, R. F.; Chen, Z.; Doroudi, S.; Lee, Y. L.; Izatt, G.; Wittman, S.; Srinivas, N.; Woods, D.; Winfree, E.; Qian, L., A cargo-sorting DNA robot. *Science* **2017,** *357* (6356).
9. Willner, E. M.; Kamada, Y.; Suzuki, Y.; Emura, T.; Hidaka, K.; Dietz, H.; Sugiyama, H.; Endo, M., Single-Molecule Observation of the Photoregulated Conformational Dynamics of DNA Origami Nanoscissors. *Angewandte Chemie International Edition* **2017,** *56* (48), 15324-15328.
10. Hu, L.; Vecchiarelli, A. G.; Mizuuchi, K.; Neuman, K. C.; Liu, J., Directed and Persistent Movement Arises from Mechanochemistry of the ParA/ParB System. *Proceedings of the National Academy of Sciences* **2015,** *112* (51), E7055.
11. Hu, L.; Vecchiarelli, A. G.; Mizuuchi, K.; Neuman, K. C.; Liu, J., Brownian Ratchet Mechanism for Faithful Segregation of Low-Copy-Number Plasmids. *Biophysical Journal* **2017,** *112* (7), 1489-1502.
12. Kovacic, S.; Samii, L.; Curmi, P. M. G.; Linke, H.; Zuckermann, M. J.; Forde, N. R., Design and Construction of the Lawnmower, an Artificial Burnt-Bridges Motor. *IEEE Transactions on NanoBioscience* **2015,** *14* (3), 305-312.
13. Nakamura, A.; Okazaki, K.-i.; Furuta, T.; Sakurai, M.; Iino, R., Processive Chitinase Is Brownian Monorail Operated by Fast Catalysis After Peeling Rail from Crystalline Chitin. *Nature Communications* **2018,** *9* (1), 3814.
14. Sherman, W. B.; Seeman, N. C., A Precisely Controlled DNA Biped Walking Device. *Nano Letters* **2004,** *4* (7), 1203-1207.
15. Shin, J. S.; Pierce, N. A., A Synthetic DNA Walker for Molecular Transport. *J. Am. Chem. Soc.* **2004,** *126*, 10834.
16. Yin, P.; Yan, H.; Daniell, X. G.; J.Turberfield, A.; John H Reif, A Unidirectional DNA Walker That Moves Autonomously along a Track *Angewandte Chemie International Edition* **2004,** *43* (37), 4906-4911.

17. Bath, J.; Green, S. J.; Turberfield, A. J., A Free-Running DNA Motor Powered by a Nicking Enzyme. *Angewandte Chemie International Edition* **2005,** *44* (28), 4358-4361.
18. Lund, K.; Manzo, A. J.; Dabby, N.; Michelotti, N.; Johnson-Buck, A.; Nangreave, J.; Taylor, S.; Pei, R.; Stojanovic, M. N.; Walter, N. G.; Winfree, E.; Yan, H., Molecular Robots Guided by Prescriptive Landscapes. *Nature* **2010,** *465* (7295), 206-10.
19. Cha, T.-G.; Pan, J.; Chen, H.; Salgado, J.; Li, X.; Mao, C.; Choi, J. H., A Synthetic DNA Motor That Transports Nanoparticles along Carbon Nanotubes. *Nature Nanotechnology* **2013,** *9* (1), 39.
20. Samii, L.; Blab, G. A.; Bromley, E. H. C.; Linke, H.; Curmi, P. M. G.; Zuckermann, M. J.; Forde, N. R., Time-Dependent Motor Properties of Multipedal Molecular Spiders. *Physical Review E* **2011,** *84* (3), 031111.
21. Tomov, T. E.; Tsukanov, R.; Glick, Y.; Berger, Y.; Liber, M.; Avrahami, D.; Gerber, D.; Nir, E., DNA Bipedal Motor Achieves a Large Number of Steps Due to Operation Using Microfluidics-Based Interface. *ACS Nano* **2017,** *11* (4), 4002-4008.
22. Jung, C.; Allen, P. B.; Ellington, A. D., A Stochastic DNA Walker That Traverses a Microparticle Surface. *Nature Nanotechnology* **2016,** *11* (2), 157-163.
23. Yao, D.; Bhadra, S.; Xiong, E.; Liang, H.; Ellington, A. D.; Jung, C., Dynamic Programming of a DNA Walker Controlled by Protons. *ACS Nano* **2020,** *14* (4), 4007-4013.
24. Jung, C.; Allen, P. B.; Ellington, A. D., A Simple, Cleated DNA Walker That Hangs on to Surfaces. *ACS Nano* **2017,** *11* (8), 8047-8054.
25. Yehl, K.; Mugler, A.; Vivek, S.; Liu, Y.; Zhang, Y.; Fan, M.; Weeks, E. R.; Salaita, K., High-Speed DNA-Based Rolling Motors Powered by RNase H. *Nat Nano* **2016,** *11* (2), 184-190.
26. Blanchard, A. T.; Bazrafshan, A. S.; Yi, J.; Eisman, J. T.; Yehl, K. M.; Bian, T.; Mugler, A.; Salaita, K., Highly Polyvalent DNA Motors Generate 100+ pN of Force *via* Autochemophoresis. *Nano Letters* **2019,** *19* (10), 6977-6986.
27. Bazrafshan, A.; Meyer, T. A.; Su, H.; Brockman, J. M.; Blanchard, A. T.; Piranej, S.; Duan, Y.; Ke, Y.; Salaita, K., Tunable DNA Origami Motors Translocate Ballistically over μm Distances at nm/s Speeds. *Angewandte Chemie International Edition* **2020,** *59* (24), 9514-9521.
28. Wang, P.; Meyer, T. A.; Pan, V.; Dutta, P. K.; Ke, Y., The Beauty and Utility of DNA Origami. *Chem* **2017,** *2* (3), 359-382.
29. Strauss, M. T.; Schueder, F.; Haas, D.; Nickels, P. C.; Jungmann, R., Quantifying Absolute Addressability in DNA Origami With Molecular Resolution. *Nature Communications* **2018,** *9* (1), 1600.
30. Lin, Z.; Strother, T.; Cai, W.; Cao, X.; Smith, L. M.; Hamers, R. J., DNA Attachment and Hybridization at the Silicon (100) Surface. *Langmuir* **2002,** *18* (3), 788-796.
31. Liu, B.; Liu, J., Methods for Preparing DNA-Functionalized Gold Nanoparticles, a Key Reagent of Bioanalytical Chemistry. *Analytical Methods* **2017,** *9* (18), 2633-2643.
32. Long, H.; Kudlay, A.; Schatz, G. C., Molecular Dynamics Studies of Ion Distributions for DNA Duplexes and DNA Clusters: Salt Effects and Connection to DNA Melting. *The Journal of Physical Chemistry B* **2006,** *110* (6), 2918-2926.
33. Hill, H. D.; Mirkin, C. A., The Bio-Barcode Assay for the Detection of Protein and Nucleic Acid Targets Using DTT-Induced Ligand Exchange. *Nature Protocols* **2006,** *1* (1), 324-336.

34. Liu, B.; Liu, J., Freezing Directed Construction of Bio/Nano Interfaces: Reagentless Conjugation, Denser Spherical Nucleic Acids, and Better Nanoflares. *Journal of the American Chemical Society* **2017,** *139* (28), 9471-9474.
35. Heuer-Jungemann, A.; Kirkwood, R.; El-Sagheer, A. H.; Brown, T.; Kanaras, A. G., Copper-Free Click Chemistry as an Emerging Tool for the Programmed Ligation of DNA-Functionalised Gold Nanoparticles. *Nanoscale* **2013,** *5* (16), 7209-7212.
36. Harimech, P. K.; Gerrard, S. R.; El-Sagheer, A. H.; Brown, T.; Kanaras, A. G., Reversible Ligation of Programmed DNA-Gold Nanoparticle Assemblies. *Journal of the American Chemical Society* **2015,** *137* (29), 9242-9245.
37. Kyriazi, M.-E.; Giust, D.; El-Sagheer, A. H.; Lackie, P. M.; Muskens, O. L.; Brown, T.; Kanaras, A. G., Multiplexed mRNA Sensing and Combinatorial-Targeted Drug Delivery Using DNA-Gold Nanoparticle Dimers. *ACS Nano* **2018,** *12* (4), 3333-3340.
38. Deal, B. R.; Ma, R.; Ma, V. P.-Y.; Su, H.; Kindt, J. T.; Salaita, K., Engineering DNA-Functionalized Nanostructures to Bind Nucleic Acid Targets Heteromultivalently with Enhanced Avidity. *Journal of the American Chemical Society* **2020,** *142* (21), 9653-9660.
39. Saxton, M. J.; Jacobson, K., Single-Particle Tracking:Applications to Membrane Dynamics. *Annual Review of Biophysics and Biomolecular Structure* **1997,** *26* (1), 373-399.
40. Sbalzarini, I. F.; Koumoutsakos, P., Feature Point Tracking and Trajectory Analysis for Video Imaging in Cell Biology. *Journal of Structural Biology* **2005,** *151* (2), 182-195.
41. Michelotti, N.; de Silva, C.; Johnson-Buck, A. E.; Manzo, A. J.; Walter, N. G., A Bird's Eye View Tracking Slow Nanometer-Scale Movements of Single Molecular Nano-Assemblies. *Methods Enzymol* **2010,** *475*, 121-48.
42. Tarantino, N.; Tinevez, J.-Y.; Crowell, E. F.; Boisson, B.; Henriques, R.; Mhlanga, M.; Agou, F.; Israël, A.; Laplantine, E., TNF and IL-1 Exhibit Distinct Ubiquitin Requirements for Inducing NEMO–IKK Supramolecular Structures. *Journal of Cell Biology* **2014,** *204* (2), 231-245.
43. Twelvetrees, Alison E.; Pernigo, S.; Sanger, A.; Guedes-Dias, P.; Schiavo, G.; Steiner, Roberto A.; Dodding, Mark P.; Holzbaur, Erika L. F., The Dynamic Localization of Cytoplasmic Dynein in Neurons Is Driven by Kinesin-1. *Neuron* **2016,** *90* (5), 1000-1015.
44. Korosec, C. S.; Sivak, D. A.; Forde, N. R., Apparent Superballistic Dynamics in One-Dimensional Random Walks with Biased Detachment. *Physical Review Research* **2020,** *2* (3), 033520.
45. Korosec, C. S.; Zuckermann, M. J.; Forde, N. R., Dimensionality-Dependent Crossover in Motility of Polyvalent Burnt-Bridges Ratchets. *Physical Review E* **2018,** *98* (3), 032114.
46. Sarah J. Hurst; Abigail K. R. Lytton-Jean, a.; Mirkin*, C. A., Maximizing DNA Loading on a Range of Gold Nanoparticle Sizes. **2006**.
47. Sims, D. W.; Southall, E. J.; Humphries, N. E.; Hays, G. C.; Bradshaw, C. J. A.; Pitchford, J. W.; James, A.; Ahmed, M. Z.; Brierley, A. S.; Hindell, M. A.; Morritt, D.; Musyl, M. K.; Righton, D.; Shepard, E. L. C.; Wearmouth, V. J.; Wilson, R. P.; Witt, M. J.; Metcalfe, J. D., Scaling Laws of Marine Predator Search Behaviour. *Nature* **2008,** *451* (7182), 1098-1102.
48. Viswanathan, G. M.; Afanasyev, V.; Buldyrev, S. V.; Murphy, E. J.; Prince, P. A.; Stanley, H. E., Lévy Flight Search Patterns of Wandering Albatrosses. *Nature* **1996,** *381* (6581), 413-415.
49. Harris, T. H.; Banigan, E. J.; Christian, D. A.; Konradt, C.; Tait Wojno, E. D.; Norose, K.; Wilson, E. H.; John, B.; Weninger, W.; Luster, A. D.; Liu, A. J.; Hunter, C. A.,

Generalized Lévy Walks and the Role of Chemokines in Migration of Effector CD8+ T Cells. *Nature* **2012,** *486* (7404), 545-548.
50. Ariel, G.; Rabani, A.; Benisty, S.; Partridge, J. D.; Harshey, R. M.; Be'er, A., Swarming bacteria migrate by Lévy Walk. *Nature Communications* **2015,** *6* (1), 8396.
51. Zanchet, D.; Micheel, C. M.; Parak, W. J.; Gerion, D.; Alivisatos, A. P., Electrophoretic Isolation of Discrete Au Nanocrystal/DNA Conjugates. *Nano Letters* **2001,** *1* (1), 32-35.
52. Liu, B.; Liu, J., Freezing-Driven DNA Adsorption on Gold Nanoparticles: Tolerating Extremely Low Salt Concentration but Requiring High DNA Concentration. *Langmuir* **2019**, 35, 19, 6476–6482

Table of contents artwork